# He-LiF surface interaction potential from fast atom diffraction

A. Schüller,[1] H. Winter,[1] M. S. Gravielle,[2,3] J. M. Pruneda,[4] and J. E. Miraglia[2,3]

[1]*Institut für Physik, Humboldt Universität zu Berlin, Newtonstrasse 15, D-12489 Berlin-Adlershof, Germany*
[2]*Instituto de Astronomía y Física del Espacio, Consejo Nacional de Investigaciones Científicas y Técnicas, Casilla de Correo 67,
Sucursal 28, C1428EGA Buenos Aires, Argentina*
[3]*Departamento de Física, Facultad de Ciencias Exactas y Naturales, Universidad de Buenos Aires, Buenos Aires, Argentina*
[4]*Centre d'Investigació en Nanociència i Nanotecnología-CIN2 (CSIC-ICN), Campus UAB, 08193 Bellaterra, Spain*

Diffraction patterns produced by grazing scattering of fast atoms from insulator surfaces are used to examine the atom-surface interaction. The method is applied to He atoms colliding with a LiF(001) surface along axial crystallographic channels. The projectile-surface potential is obtained from an accurate density-functional theory calculation, which includes polarization effects and surface relaxation. For the description of the collision process we employ the surface eikonal approximation, which takes into account quantum interference between different projectile paths. The dependence of projectile spectra on the parallel and perpendicular incident energies is experimentally and theoretically analyzed, demonstrating the range of applicability of the proposed model.

## I. INTRODUCTION

Diffraction of thermal atoms from crystal surfaces has been extensively studied over the years [1–11], becoming a common tool for surface analysis. Recently, new experiments [12–15] have shown interference effects also for grazing scattering of fast atoms from surfaces, where classical mechanics was supposed to be adequate. This unexpected diffraction phenomenon was found to be very sensitive to the projectile-surface interaction [14–18], which opens the way for a method to probe surface potentials with high accuracy.

The aim of this work is to find out to what extent surface potentials derived from state-of-art *ab initio* methods are capable of reproducing experimental diffraction patterns for grazing scattering of swift He atoms from a LiF(001) surface. The He-LiF surface interaction is derived here by using the SIESTA [19] implementation of the density-functional theory (DFT), which is a self-consistent method for performing first-principles calculations on systems with a large number of atoms. This DFT method has been successfully used to study a variety of nanoscale problems [20]. In order to describe the interference process, we employ a distorted-wave model—the surface eikonal approximation [16]—using the eikonal wave function to represent the elastic collision with the surface, while the motion of the fast projectile is described classically by considering axially channeled trajectories for different initial conditions. The surface eikonal approximation is valid for small de Broglie wavelengths of incident atoms [21], as considered here, which are several orders of magnitude smaller than the interatomic spacings in the crystal. This method was shown to provide an adequate description of the interference effects for atoms colliding with insulator surfaces under axial surface channeling [22].

Eikonal projectile angular distributions derived from using the DFT surface potential are compared with the experiment for different energies of incident projectiles. From this comparison, we deduce the validity range of the potential model, which involves polarization and surface rumpling.

The paper is organized as follows. The experimental method and the theoretical formalism are summarized in Secs. II and III, respectively. Results are presented and discussed in Sec. IV, and in Sec. V, we outline our conclusions. Atomic units (a.u.) are used unless otherwise stated.

## II. EXPERIMENTAL METHOD

In our experiments, we have scattered neutral $^3$He and $^4$He atoms with kinetic energies $E_i$ ranging from 0.3 to 25 keV from a clean and flat LiF(001) surface at room temperature under grazing angles of incidence $0.4 < \theta_i < 1.5°$. Fast He$^+$ ion beams were produced in a 10 GHz electron cyclotron resonance (ECR) ion source (Nanogan Pantechnique, Caen, France). The neutralization of the He$^+$ ions was achieved via charge transfer in a gas cell mounted in the beam line of the accelerator operating with He gas and subsequent deflection of remaining ions by an electric field. A base pressure of some $10^{-11}$ mbar was achieved in our ultrahigh vacuum chamber by a turbomolecular pump in series with a titanium sublimation pump, where the pressure gradient with respect to the beam line of the accelerator was maintained by two differential pumping stages. Pairs of slits at both ends of these stages were used for the collimation of the incident beam to a divergence of $<0.03°$. This high collimation is necessary for diffraction in order to maintain the degree of coherence in the scattering process from LiF(001).

The LiF(001) surface was prepared by cycles of grazing sputtering with 25 keV Ar$^+$ ions at 250 °C where the ionic conductivity of LiF is sufficiently enhanced in order to avoided macroscopic charging up and subsequent annealing to temperatures of about 350 °C. The scattering experiments were performed in the regime of axial surface channeling, i.e., the azimuthal setting of the surface plane was chosen such that the direction of the incident beam was parallel with atomic strings along low indexed directions in the surface plane.

Two-dimensional angular distributions of scattered projectiles were recorded by means of a commercially available position-sensitive multichannelplate detector (MCP) with a delay-line anode (DLD40, Roentdek Handels GmbH) located 66 cm behind the target. This provides a simple and very efficient procedure for recording data where complete diffraction patterns as shown below can be recorded in a time of typically minutes. Since only about $10^4$ He atoms per second hit the target surface, fast atom diffraction is nondestructive and can be applied in studies on insulator surfaces (neutral projectiles) [12,13], as well as adsorption phenomena at metal surfaces [15,18].

Since aside from the absolute angular positions of diffraction spots, their relative intensities are important here, one has to carefully correct the recorded diffraction patterns with respect to inhomogeneities in the detection efficiency across the sensitive area of the MCP. This correction is performed by means of a wobbling technique where the projectile beam is scanned across the MCP active area with two orthogonal oriented electric fields using frequencies in the kHz domain.

## III. THEORETICAL MODEL

When an atomic projectile ($P$) impinges under grazing incidence on a crystal surface ($S$) the $T$-matrix element associated with the elastic scattering can be defined in terms of the scattering state of the projectile, $\Psi_i^+$, as

$$T_{if} = \int d\vec{R}_P \Phi_f^*(\vec{R}_P) V_{SP}(\vec{R}_P)\Psi_i^+(\vec{R}_P), \qquad (1)$$

where $V_{SP}$ is the surface-projectile interaction, $\vec{R}_P$ denotes the position of the center of mass of the incident atom, and $\Phi_j(\vec{R}_P)=(2\pi)^{-3/2}\exp(i\vec{K}_j\cdot\vec{R}_P)$, with $j=i(f)$, being the initial (final) unperturbed wave function and $\vec{K}_{i(f)}$ the initial (final) projectile momentum. Taking into account that in the range of impact energies the de Broglie wavelength of the incident projectile, $\lambda=2\pi/K_i$, is sufficiently short compared to the characteristic distance of the surface potential, we approximate the scattering state $\Psi_i^+$ by means of the eikonal Maslov wave function [21] as follows:

$$\Psi_i^+(\vec{\mathcal{R}}_P) \simeq \chi_i^{(eik)+}(\vec{\mathcal{R}}_P) = \Phi_i(\vec{\mathcal{R}}_P)\exp[-i\eta(\vec{\mathcal{R}}_P)], \qquad (2)$$

where

$$\eta(\vec{\mathcal{R}}_P(t)) = \int_{-\infty}^{t} dt' V_{SP}(\vec{\mathcal{R}}_P(t')) + \phi_M \qquad (3)$$

is the eikonal Maslov phase, which depends on the classical position of the incident atom $\vec{\mathcal{R}}_P$ at a given time $t$. This phase includes the Maslov correction term $\phi_M=\nu\pi/2$ that takes into account the phase change suffered by a wave as it passes through a focus, with $\nu$ the Maslov index defined as in Refs. [23]. Note that the dependence of the eikonal phase on the component of the velocity parallel to the surface becomes evident from Eq. (3) by changing the integration variable by the component of $\vec{\mathcal{R}}_P$ along the incidence channel. By inserting Eq. (2) in Eq. (1), after some algebra, the eikonal transition matrix reads [16]

$$T_{if}^{(eik)} = \int d\vec{R}_{os}\, a_{if}(\vec{R}_{os}), \qquad (4)$$

where $\vec{R}_{os}$ determines the initial position of the projectile on the surface plane and

$$a_{if}(\vec{R}_{os}) = \frac{1}{(2\pi)^3}\int_{-\infty}^{+\infty} dt|v_z(\vec{\mathcal{R}}_P)|$$

$$\times\exp[-i\vec{Q}\cdot\vec{\mathcal{R}}_P - i\eta(\vec{\mathcal{R}}_P)]V_{SP}(\vec{\mathcal{R}}_P) \qquad (5)$$

is the transition amplitude associated with the classical path $\vec{\mathcal{R}}_P(\vec{R}_{os},t)$. In Eq. (5), $\vec{Q}=\vec{K}_f-\vec{K}_i$ is the projectile momentum transfer and $v_z(\vec{\mathcal{R}}_P)$ denotes the component of the projectile velocity perpendicular to the surface plane, with $\hat{z}$ directly along the surface normal, toward the vacuum region.

The differential probability, per unit of surface area, for elastic scattering with final momentum $\vec{K}_f$ in the direction of the solid angle $\Omega_f\equiv(\theta_f,\varphi_f)$, is obtained from Eq. (4) as $dP/d\Omega_f=(2\pi)^4 m_P^2|\tilde{T}_{if}^{(eik)}|^2$, where $\tilde{T}_{if}^{(eik)}$ denotes the eikonal $T$-matrix element, normalized per unit area, $m_P$ is the projectile mass, and $\theta_f$ and $\varphi_f$ are the final polar and azimuthal angles, respectively, with $\varphi_f$ measured with respect to the $\hat{x}$ axis, along the incidence direction in the surface plane. Details are given in Refs. [16,22].

### Projectile-surface interaction

The surface potential was determined by performing first-principles calculations for the LiF(001) surface. We used the SIESTA [19] implementation of density-functional theory within the local density approximation (LDA) [24] to obtain the effective interaction potential between a He atom and a slab of 10 atomic planes of LiF. Periodic boundary conditions were used in the (001) plane, and in order to prevent the interaction between images of the He atoms, a $\sqrt{(2)}\times\sqrt{(2)}$ supercell was considered in the (001) plane, giving a total of $112+1$ atoms in the simulation box.

We model the core electrons with norm-conserving pseudopotentials of the Troullier-Martins type [25], describing valence electrons with numerical double-*zeta* polarized atomic orbitals as the basis set. We explicitly included semi-core states for Li ($1s^2$) in the valence band and added two extra layers of "ghost orbitals" with the same quality, centered at the ideal positions of Li and F above the surface, to increase the basis set description of the surface electronic wave-functions.

The structure was optimized until the forces on all atoms were smaller than 0.03 eV/Å. The slight underestimation for the in-plane lattice constant obtained in our slab geometry (3.94 Å, experimental 4.02 Å [9]) is typical of LDA calculations. Different relaxation of the Li and F atoms at the surface called rumpling is apparent in the first two atomic layers, with F atoms in the surface plane being slightly pushed out and Li atoms slightly depressed by a distance $d_1$ measured with respect to the unreconstructed surface. For the topmost atomic layer, we obtained $d_1=0.046$ a.u., while the displacement corresponding to the second layer is substantially smaller and in opposite direction ($d_2=-0.010$ a.u.).
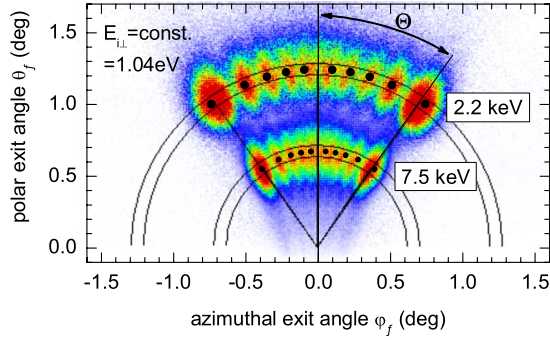
FIG. 1. (Color online) Two-dimensional intensity distributions, as recorded with a position-sensitive detector, for $^4$He atoms scattered from LiF(001) along a $\langle 110 \rangle$ direction with two different projectile energies, $E_i = 2.2$ and 7.5 keV, but with the same perpendicular energy ($E_{i\perp} = 1.04$ eV). Color code: red=high and blue=low intensity. Positions of rainbow angles $\Theta_{rb}$ are indicated by straight lines. Black dots represent theoretical positions of maxima from the surface eikonal model.

These values are slightly higher than those reported from a low energy electron diffraction analysis [26] but still within the experimental errors.

The surface potential $V(z)$ for a given position $(x,y)$ on the surface plane was obtained from calculations of the total energy of the system composed by the LiF slab and the He atom placed a distance $z$ from the last atomic layer of the slab (taken as the average between Li and F positions). The standard correction [27] due to basis set superposition errors (BSSE) was considered for the computed $V(z)$

$$V(z) = E[\text{LiF} + \text{He}(z)] - E[\text{He}(z)]^{\text{LiF}} - E[\text{LiF}]^{\text{He}(z)}, \quad (6)$$

where $E[A]^X$ denotes the energy of the system $A$ considering not only the basis orbitals of $A$, but also those that correspond to the subsystem $X$. Once $V(z)$ is known for selected nine in-plane high-symmetry positions in a mesh of $z$ points, an interpolation scheme is used to derive $V_{SP}(\vec{R})$ at any point in the vacuum region.

## IV. RESULTS

Experimental angular distributions of He$^0$ projectiles elastically scattered from a LiF(001) surface under axial surface channeling conditions are presented here as a benchmark for the DFT projectile-surface potential.

First, we analyze the dependence of final projectile distributions on the incidence energy $E_i$, split into two terms $E_i = E_{i\parallel} + E_{i\perp}$, where $E_{i\parallel} = E_i \cos^2 \theta_i$ ($E_{i\perp} = E \sin^2 \theta_i$) is associated with the component of the initial velocity parallel (perpendicular) to the axial channel, with $\theta_i$ being the incidence angle measured with respect to the surface plane. In Fig. 1, we show diffraction patterns for $^4$He atoms impinging along the $\langle 110 \rangle$ direction with two different energies—$E_i = 2.2$ and 7.5 keV—but via the settings of the angle of incidence with the same perpendicular energy, $E_{i\perp} = 1.04$ eV. In both cases, the distribution for scattered projectiles lies inside an annulus of radius $\theta_i$, presenting maxima symmetrically placed with respect to the incidence direction (i.e., $\varphi_f = 0$). The high intensity for the outermost peaks (marked with lines) is due to rainbow scattering under the rainbow angle $\Theta_{rb}$ at maximal deflection, which can be explained classically. Between the outer rainbow peaks further peaks show up, which can be explained as quantum mechanical diffraction effects in close analogy to the origin of supernumerary rainbows [14]. Supernumerary rainbows originate from quantum interference between projectiles that follow different classical pathways with the same final momentum. The order $m$ of a supernumerary corresponds to the multiple of $\lambda$ in path length difference for constructive interference. For grazing scattering, such structures in the angular distributions were predicted by Andreev [28]. The black dots in Fig. 1 represent the theoretical positions of the maxima from the eikonal model, which closely agree with the experimental data.
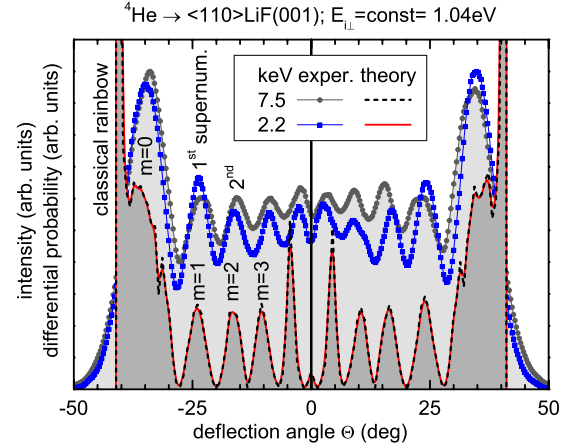
In Fig. 2, we show the intensity inside the annulus of radius $\theta_i$ from Fig. 1 as a function of the deflection angle $\Theta$, defined as $\Theta = \arctan(\varphi_f / \theta_f)$. Position and number of the supernumerary maxima are independent of $E_i$ at the same $E_{i\perp}$. Similar structures are predicted by the eikonal model, although in the vicinity of the classical rainbow angle $\Theta_{rb}$ the relative intensity is overestimated. This has its origin in the eikonal model, which is a semiclassical method based on classically calculated trajectories, showing a sharp maximum at the classical rainbow, where intensity increases sharply for $\Theta \to \Theta_{rb}$ and is zero for $\Theta > \Theta_{rb}$. In a more elaborate quantum treatment, the classical rainbow peak will be replaced by a smoothed maximum for $m = 0$ at $\Theta < \Theta_{rb}$, with decaying intensity on the dark side of the classical rainbow $\Theta > \Theta_{rb}$ [28–30]. The maximum for $m = 0$ is the "quantum surface rainbow" [31].

Just like in the experiment, eikonal patterns as a function of the deflection angle $\Theta$ are independent of $E_i$ for the same $E_{i\perp}$. This is more evident from Fig. 3, where deflection angles corresponding to supernumerary rainbows are plotted as a function of the total energy $E_i$ while keeping $E_{i\perp}$ constant. Even though $V_{SP}(\vec{R})$ takes into account the complete



FIG. 2. (Color online) Projected intensities inside annuluses in Fig. 1, as a function of the deflection angle $\Theta$, for $E_i = 7.5$ keV (gray circles) and 2.2 keV (blue squares) and corresponding differential probabilities derived from the surface eikonal approach (black dashed and red full curves). $m$ denotes the order of the supernumerary rainbow.
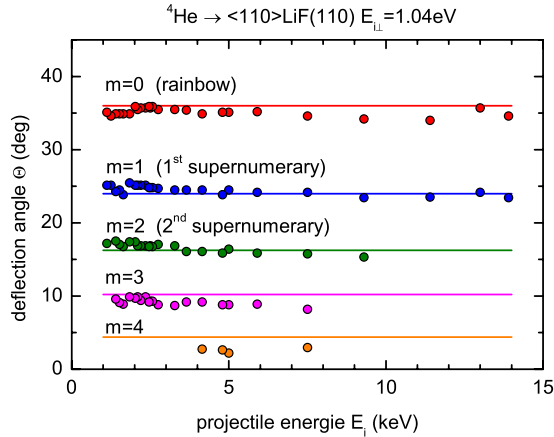
FIG. 3. (Color online) Deflection angles $\Theta$ corresponding to maxima of angular distributions, as a function of the projectile energy $E_i$, for $^4$He atoms scattered from LiF(001) along the direction $\langle 110 \rangle$. The perpendicular energy is kept as a constant ($E_{i\perp}$ =1.04 eV). Circles, experimental data; curves, quantum rainbow $m=0$ and supernumerary rainbows $m=1$ to 4 derived within the surface eikonal approximation.

corrugation on the surface plane, without averaging the projectile-surface potential along the incidence direction, the eikonal projectile distribution is practically unaffected by the modulation of the potential along the channel. Thus, the differential probability $dP/d\Theta$ is independent of $E_{i\parallel}$ for a given perpendicular energy. On the other hand, the positions of supernumerary maxima are found to be extremely sensitive to the shape of the surface potential across the channel, especially for higher orders $m$, which correspond to small deflection angles [14,16,17,22]. From Fig. 3, we conclude that the DFT surface potential reproduces fairly well the angular positions of the supernumeraries.

Different perpendicular energies $E_{i\perp}$ probe a different $z$ range of $V_{SP}$. To investigate in detail the atom-surface potential across the $\langle 110 \rangle$ channel, we plot in Fig. 4 the angular positions of maxima of the experimental distribution as a function of $E_{i\perp}$ ranging from 0.03 to 3 eV. In this case, $^3$He projectiles are used. For low perpendicular energies, i.e., $E_{i\perp} \lesssim 1$ eV, the experimental spectra show maxima at Bragg angles $\Theta_n$, which fulfill the condition

$$d \sin \Theta_n = n\lambda_\perp, \qquad (7)$$

$d$ being the width of the axial channel, $n$ the diffraction order, and $\lambda_\perp = 2\pi/K_{iz}$ the de Broglie wavelength associated with the perpendicular motion. As discussed in Refs. [14,32], interference patterns for grazing scattering stem from two different mechanisms. The first one, related to the supernumerary rainbows, is produced by the interference of trajectories whose initial positions $\vec{R}_{os}$ differ by a distance smaller than $d$, carrying information on the shape of the interaction potential across the channel. The second one originates from the interference of trajectories whose initial positions $\vec{R}_{os}$ are separated by the spacial lattice periodicity $d$, resulting in "Bragg peaks" providing information on the spacing between surface atoms. The intensities of Bragg peaks depend on the
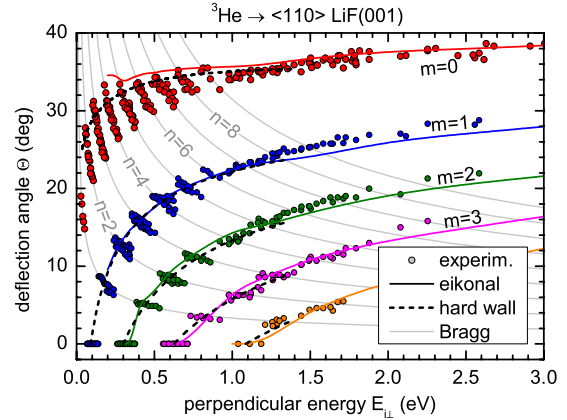


FIG. 4. (Color online) Similar to Fig. 3, but as function of the perpendicular energy $E_{i\perp}$, for $^3$He atoms scattered from LiF(001) along the direction $\langle 110 \rangle$. Full colored curves, quantum rainbow $m=0$, and supernumerary rainbows $m=1$ to 4 derived within the surface eikonal approximation based on the present DFT potential; dashed curves, positions of supernumerary rainbows in hard-wall approximation [Eq. (8)] using the effective corrugation $\Delta z$ of the DFT potential across the $\langle 110 \rangle$ channel; thin gray curves, theoretical positions of maxima of order $n$ from Bragg condition [Eq. (7)].

position of the supernumeraries. The Bragg peak of order $n$, which is closest to the angular position of a supernumerary of order $m$, is most intense. Since the Bragg angles $\Theta_n$ decrease with $E_{i\perp}$ while the angular position of the supernumeraries increases, the order $n$ of the intense Bragg peak increases successively.

Signatures of both interference processes can be observed in the simulated spectrum as well. In Fig. 5, the eikonal probability $dP/d\Theta$ is plotted as a function of the deflection
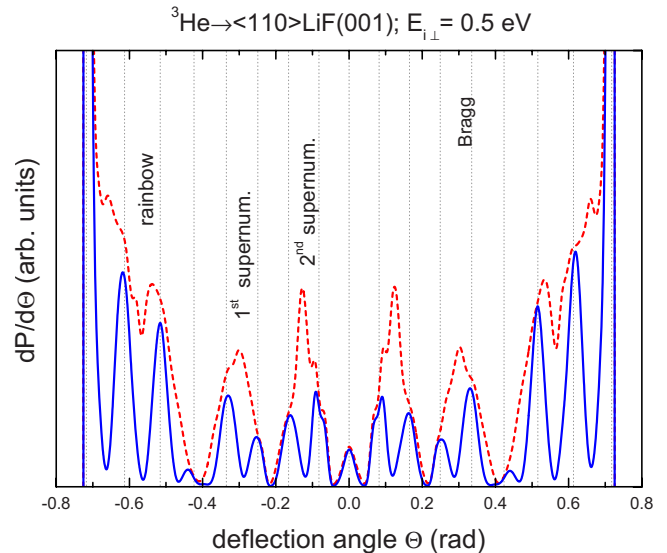


FIG. 5. (Color online) Eikonal results for $^3$He atoms scattered from LiF(001) along the direction $\langle 110 \rangle$ for the perpendicular energy $E_{i\perp}$=0.5 eV. Dashed (red) line, eikonal differential probability derived by integrating the initial position over an unit cell; solid (blue) line, similar by using an extended integration area, as explained in the text. Dotted vertical lines, theoretical peak positions based on Bragg condition [Eq. (7)].
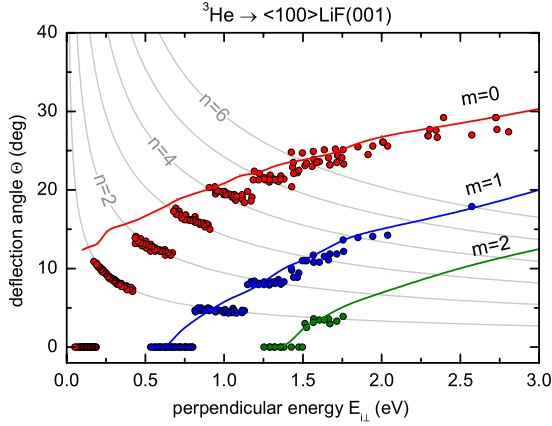
FIG. 6. (Color online) Similar to Fig. 4, but for scattering along the $\langle 100 \rangle$ direction.

angle for $E_{i\perp}=0.5$ eV. If in Eq. (4) the initial projectile position $\vec{R}_{os}$ is integrated over a unit cell, supernumerary maxima are present in the angular projectile distribution only. But when the integration area is extended in order to include the first order nearest neighbor target ions, the eikonal spectrum displays internal structures in the supernumerary maxima, which stem from resolved Bragg peaks.

Since we are interested in studying the modulation of the potential inside an unit cell, we have plotted in Fig. 4 eikonal curves corresponding to the center of supernumerary maxima, neglecting the Bragg interference that appears as a superimposed structure at low perpendicular energies. The eikonal curves obtained by using the DFT atom-surface interaction follow closely the experimental results for supernumeraries $m=1$ to $m=4$ with only slight deviations for the quantum rainbow $m=0$ at low $E_{i\perp}$. Supernumerary rainbows are sensitive to the corrugation of the equipotential surfaces but not to their positions. Each potential with the same effective corrugation along the $\langle 110 \rangle$ direction would agree as well. In order to demonstrate the consistency of our potential, we compare the theoretical results with the experiment for a further (symmetrically different) channeling direction.

In Fig. 6, we show a comparison of experimental supernumerary rainbows with eikonal results for scattering of $^3$He along a $\langle 100 \rangle$ direction of LiF(001). The eikonal curves with the DFT potential agree with the experimental values except for $m=0$ at low energies $E_{i\perp} \lesssim 1.0$ eV. Also for this case, the eikonal approximation as a semiclassical theory fails in the vicinity of the classical rainbow $\Theta_{rb}$. The angular position of the quantum rainbow $m=0$ is smaller than the classical rainbow angle $\Theta_{rb}$ when $\lambda_\perp$ becomes large [31]. Since the intensity at $\Theta_{rb}$ is overestimated, the peak maximum $m=0$ is shifted to larger deflection angles at lower $E_{i\perp}$. For a correct description of the intensity at $\Theta_{rb}$, a "uniform approximation" [29,30] is necessary, but supernumeraries are not affected by this deficiency. Since the positions of the supernumeraries agree well in both channeling directions and since a change in the corrugation of the He-LiF(001) interaction potential by 0.02 Å induces a clear shift in the position of the supernumeraries [14,22], we conclude that the DFT He-LiF(001) potential is adequate here.

By employing the hard-wall model from Garibaldi *et al.* [31] valid for sinusoidal small corrugated potential surfaces,

we obtain good agreement as well. Hard-wall approximations were applied successful for description of scattering of He from LiF(001) with thermal energies [2,6,33,34]. Due to the large parallel velocity of the He projectile, the effective potential is averaged along the chains of atoms in the channeling direction. The potential contours of the effective potential for scattering along $\langle 110 \rangle$ for low energies are well approximated by sine functions. For a sinusoidal hard wall, the intensity $I_n$ of a Bragg peak of order $n$ is given by

$$I_n = J_n^2 \left( \frac{\pi \Delta z}{\lambda_\perp} [1 + \cos \Theta_n] \right), \tag{8}$$

with $J_n$ being the Bessel function of order $n$, $\Theta_n = \arccos \sqrt{1 - (n\lambda_\perp/d)^2}$, the deflection angle of order $n$, and $\Delta z$ the full corrugation of the sinusoidal hard wall, i.e., the normal distance between the maximum and the minimum of an equipotential surface. In Ref. [35], it was shown that the solution given by Eq. (8) is in agreement with the exact quantum mechanical solution in a wide range of $\lambda_\perp$. Since we are interested in the angular positions of the supernumerary rainbows, we treat $n$ in Eq. (8) as $\in \mathbb{R}$ and search for the maxima of this oscillating function by searching the zeros of the derivation of Eq. (8) where for $\Delta z(E_{i\perp})$, the effective corrugation of the present DFT potential across the $\langle 110 \rangle$ channel was used. Results are displayed in Fig. 4, showing good agreement with the experiment and with the eikonal approach. This allows us to conclude that the hard-wall model is a good approximation here.

We then apply the hard-wall approximation in order to describe the different relative intensities of the Bragg peaks as shown in Fig. 7. We fit a sum of Lorentzian peaks to the diffraction pattern, where the peak positions are given by the Bragg relation [Eq. (7)]. We assume, that the peak width is the same for all diffraction spots [36]. Resulting relative peak heights are compared with the relative intensities given by Eq. (8) with $\Delta z$ as a fit parameter. The resulting intensity distributions are shown as full curves in Fig. 7. The values for $\Delta z$ obtained from the best fit are given in each panel. Since $\Delta z$ is almost constant, the differences in the intensities are due to the different de Broglie wavelength $\lambda_\perp$ only.

The effective corrugation $\Delta z$ of the potential across the $\langle 110 \rangle$ channel deduced from Bragg peak intensities for scattering of $^3$He and $^4$He under different angles of incidence is plotted as a function of the perpendicular energy $E_{i\perp}$ in Fig. 8 by open symbols. Each data point corresponds to a best fit with Eq. (8) as in Fig. 7. Although the diffraction patterns are different for the He isotopes and for different angles of incidence, the data are well described by Eq. (8) with an almost constant corrugation $\Delta z$. We compare the experimentally derived values with the effective corrugation of the present DFT potential (full curve in Fig. 8) defined as the normal distance between the maximum and minimum of the equipotential surface obtained by averaging the surface potential along the $\langle 110 \rangle$ axial channel. We observe that the theoretical curve is close to the experimental data.

In order to demonstrate the improvement by the present DFT potential upon currently available descriptions of the He-LiF(001) interaction, we show results from further calcu-

$^3$He→ <110>LiF(001) Φ$_{in}$= 0.99°

a) E$_i$= 0.35keV  λ$_\perp$= 0.508Å  Δz= 0.318Å

b) E$_i$= 0.50keV  λ$_\perp$= 0.425Å  Δz= 0.322Å

c) E$_i$= 0.65keV  λ$_\perp$= 0.372Å  Δz= 0.316Å
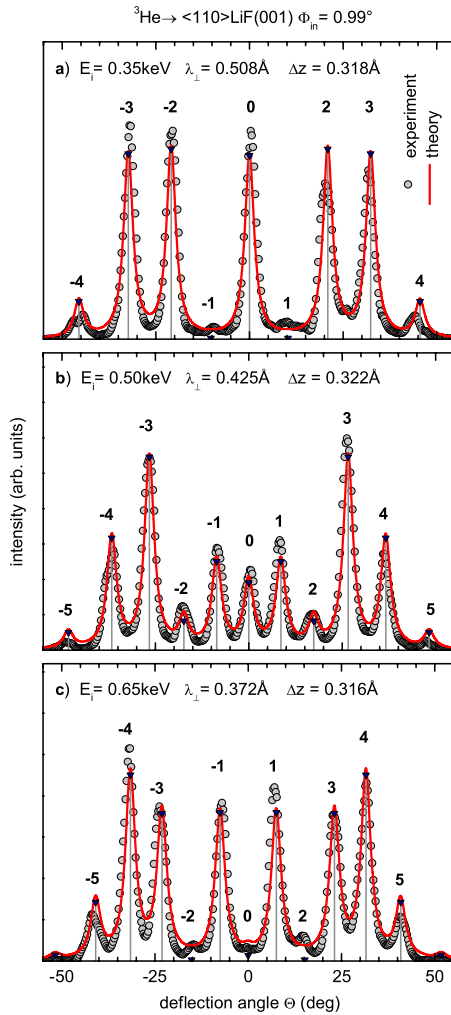
FIG. 7. (Color online) Intensity distributions as function of deflection angle $\Theta$ for scattering of $^3$He atoms from LiF(001) along $\langle 110 \rangle$ under $\theta_i = 0.99°$ with a) $E_i = 0.35$ keV, b) $E_i = 0.50$ keV, and c) $E_i = 0.65$ keV. Solid curves represent best fits to data by sum of peaks with Lorentzian lineshapes weighted by Eq. (8). Deduced best fit corrugation $\Delta z$ is given in each panel. Numbers denote order $n$ and gray bars theoretical positions of Bragg peaks from Eq. (7).

lations in Fig. 8 for comparison. The interaction potential from Celli *et al.* [8] is considered as the best available He-LiF(001) potential [10,11]. But the resulting effective corrugation in the range of some 100 meV shows a strong dependence on the perpendicular energy $E_{i\perp}$ in contrast to the experiment. We thus conclude that the potential from Celli *et al.* is not adequate for the description of the He-LiF(001) potential in the eV range. This is not in conflict with the results of Refs. [10,11], where the experiment is sensitive to the attractive potential well of the planar averaged potential in the meV range only, but not to the corrugation of the repulsive part of the interaction potential in the eV domain. The repulsive part of the Celli potential is based on self-consistent field pair potentials for He-Li$^+$ and He-F$^-$ from Ahlrichs *et al.* [38]. Due to an error in the calculation of He-F$^-$ repulsion [37], which is the dominant contribution of the repulsive part of the He-LiF(001) interaction potential, the Celli potential has to be corrected. The correct He-F$^-$
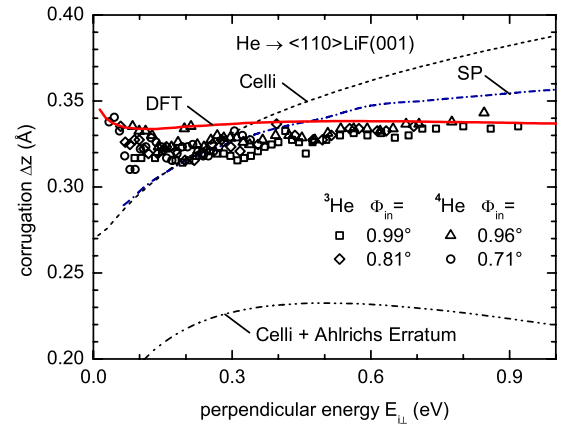


FIG. 8. (Color online) Effective corrugation $\Delta z$ of the potential across the $\langle 110 \rangle$ channel as a function of the perpendicular energy $E_{i\perp}$. Open symbols, experimentally derived results in hard-wall approximation; solid red curve, values derived from the present DFT potential; dashed curve, corrugation obtained from the interaction potential from Celli *et al.* (Ref. [8]); dashed-double dotted curve, corrugation from the potential from Celli *et al.* but with the correct He-F$^-$ pair potential from Erratum of Ahlrichs *et al.* (Ref. [37]); dashed-dotted curve, corrugation from the static potential (SP) of Ref. [16], as explained in the text.

potential [37,38] is in good agreement with recent He-F$^-$ *ab initio* pair potentials [39,40] up to several eV as well as the original He-Li$^+$ pair potential [38] agrees with recent He-Li$^+$ *ab initio* potentials [41,42] up to some eV. Nevertheless, inserting the corrected He-F$^-$ parameters in the expression for the Celli potential, the effective corrugation $\Delta z(E_{i\perp})$ in the range of some 100 meV energy deviates from the experimental results even more. The static potential of Ref. [16] (without the contribution of the projectile polarization) is obtained "pairwise additive," like the Celli potential as a sum of individual interatomic potentials, which agree for energies >0.2 eV with the *ab initio* pair potentials [40–42]. Taking into account the same rumpling as obtained by the present DFT calculation, one derives an effective corrugation fairly close to the experimental values (about 6% above), but with an underestimation for $E_{i\perp} < 0.2$ eV.

The small variation in the effective corrugation $\Delta z$ with the perpendicular energy explains why He isotopes with the same $\lambda_\perp$, but different perpendicular energies $E_{i\perp}$ produce similar diffraction patterns, even though different regions of the surface potential are probed. As observed in Fig. 9, He atoms with the same perpendicular de Broglie wavelength ($\lambda_\perp = 0.13$ Å) but different perpendicular energies ($E_{i\perp} = 1.63$ and 1.21 eV) show identical eikonal distributions, as in the experiment. The scattering processes take place indeed at different distances to the surface, but since $\lambda_\perp$ and $\Delta z(E_{i\perp})$ are the same, similar interference patterns appear.

## V. CONCLUSIONS

We have studied diffraction patterns for keV He atoms colliding under grazing incidence with a LiF(001) surface in order to test the *ab initio* surface potential, obtained from DFT by making use of the SIESTA code. Angular distributions
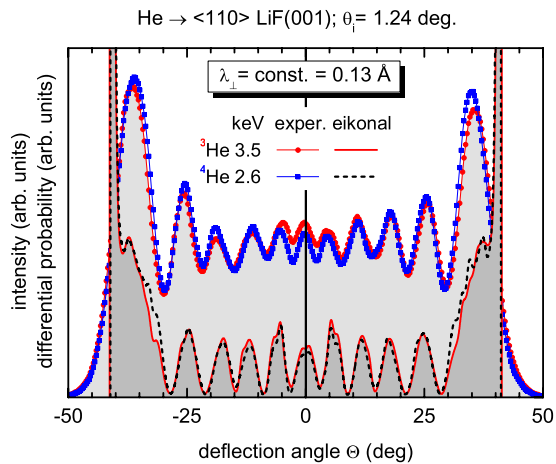
FIG. 9. (Color online) Angular distributions for He atoms scattered from LiF(001) along the direction $\langle 110 \rangle$ with $\lambda_\perp =0.13$ Å. Two different isotopes and impact energies are considered. Red circles and full curve, experimental data and eikonal results, respectively, for 3.5 keV $^3$He; blue squares and dashed curve, for 2.6 keV $^4$He.

of scattered projectiles are obtained with the DFT potential from the surface eikonal approximation, which takes into account the quantum interference in terms of the coherent superposition of transition amplitudes for different projectile paths with the same deflection angle.

For scattering along the $\langle 110 \rangle$ channel, the dependence on the parallel and perpendicular components of the impact energy was analyzed. It was found that angular distributions in terms of the deflection angle $\Theta$ are completely governed by the perpendicular energy. Diffraction spectra as a function of $\Theta$ give information on the surface potential across the incidence channel for two different mechanisms: supernumerary rainbow and Bragg interferences. We have focused here on supernumerary rainbows, which are very sensitive to the corrugation of the surface potential within a unit cell. By comparison of calculated angular spectra with experimental distributions, we concluded that the DFT model provides a good description of the surface potential for energies in the range from $E_{i\perp}=0.03$ eV up to 3 eV. The agreement between theory and experimental results for the intensity near the classical rainbow angle is poorer for smaller $E_{i\perp}$. This deficiency is attributed to the range of validity of the semiclassical models, like the eikonal approach, which treats the projectile trajectory classically.

For scattering along the $\langle 110 \rangle$ direction, the calculation in the hard-wall approximation using Eq. (8) is in good agreement with results from simulation with the soft potential based on the eikonal model.

We found that the potential from Celli *et al.* [8] is not adequate for the description of the interaction of He with LiF(001) in the eV energy domain. The DFT potential displays a constant effective corrugation for scattering along $\langle 110 \rangle$ as function of the perpendicular energy, in agreement with the experiment.

## ACKNOWLEDGMENTS

[1] N. Cabrera, V. Celli, F. O. Goodman, and R. Manson, Surf. Sci. **19**, 67 (1970).
[2] G. Boato *et al.*, J. Phys. C **6**, L394 (1973).
[3] G. Boato, P. Cantini, and L. Mattera, Surf. Sci. **55**, 141 (1976).
[4] G. Wolken, J. Chem. Phys. **58**, 3047 (1973).
[5] N. García, J. Ibáez, J. Solana, and N. Cabrera, Solid State Commun. **20**, 1159 (1976).
[6] N. García, J. Chem. Phys. **67**, 897 (1977).
[7] L. M. Hubbard and W. H. Miller, J. Chem. Phys. **78**, 1801 (1983).
[8] V. Celli, D. Eichenauer, A. Kaufhold, and J. P. Toennies, J. Chem. Phys. **83**, 2504 (1985).
[9] Y. Ekinci and J. P. Toennies, Surf. Sci. **563**, 127 (2004).
[10] A. P. Jardine *et al.*, Science **304**, 1790 (2004).
[11] D. J. Riley, A. P. Jardine, S. Dworski, G. Alexandrowicz, P. Fouquet, J. Ellis, and W. Allison, J. Chem. Phys. **126**, 104702 (2007).
[12] A. Schüller, S. Wethekam, and H. Winter, Phys. Rev. Lett. **98**, 016103 (2007).
[13] P. Rousseau, H. Khemliche, A. G. Borisov, and P. Roncin, Phys. Rev. Lett. **98**, 016104 (2007).

[14] A. Schüller and H. Winter, Phys. Rev. Lett. **100**, 097602 (2008).
[15] A. Schüller, M. Busch, S. Wethekam, and H. Winter, Phys. Rev. Lett. **102**, 017602 (2009).
[16] M. S. Gravielle and J. E. Miraglia, Phys. Rev. A **78**, 022901 (2008).
[17] F. Aigner, N. Simonović, B. Solleder, L. Wirtz, and J. Burgdörfer, Phys. Rev. Lett. **101**, 253201 (2008).
[18] A. Schüller, M. Busch, J. Seifert, S. Wethekam, H. Winter, and K. Gärtner, Phys. Rev. B **79**, 235425 (2009).
[19] J. M. Soler, E. Artacho, J. D. Gale, A. García, J. Junquera, P. Ordejón, and D. Sánchez-Portal, J. Phys.: Condens. Matter **14**, 2745 (2002).
[20] E. Artacho, E. Anglada, O. Dieguez, J. D. Gale, A. García, J. Junquera, R. M. Martin, P. Ordejón, J. M. Pruneda, D. Sánchez-Portal, and J. M. Soler, J. Phys.: Condens. Matter **20**, 064208 (2008).
[21] C. J. Joachain, *Quantum Collision Theory* (North-Holland, Amsterdam, 1979).
[22] M. S. Gravielle and J. E. Miraglia, Nucl. Instrum. Methods Phys. Res. B **267**, 610 (2009).

[23] W. F. Avrin and R. P. Merrill, Surf. Sci. **311**, 269 (1994).

[24] J. P. Perdew and A. Zunger, Phys. Rev. B **23**, 5048 (1981).

[25] N. Troullier and J. L. Martins, Phys. Rev. B **46**, 1754 (1992).

[26] J. Vogt and H. Weiss, Surf. Sci. **501**, 203 (2002).

[27] F. Boys and F. Bernardi, Mol. Phys. **19**, 553 (1970).

[28] E. A. Andreev, Russ. J. Phys. Chem. **76**, S164 (2002).

[29] M. V. Berry and K. E. Mount, Rep. Prog. Phys. **35**, 315 (1972).

[30] M. V. Berry, Proc. Phys. Soc. London **89**, 479 (1966).

[31] U. Garibaldi, A. C. Levi, R. Spadacini, and G. E. Tommei, Surf. Sci. **48**, 649 (1975).

[32] A. Schüller and H. Winter, Nucl. Instrum. Methods Phys. Res. B **267**, 628 (2009).

[33] H. Chow and E. D. Thompson, Surf. Sci. **54**, 269 (1976).

[34] N. García, J. Ibáñez, J. Solana, and N. Cabrera, Surf. Sci. **60**, 385 (1976).

[35] R. I. Masel, R. P. Merrill, and W. H. Miller, J. Chem. Phys. **65**, 2690 (1976).

[36] M. Busch, A. Schüller, S. Wethekam, and H. Winter, Surf. Sci. **603**, L23 (2009).

[37] R. Ahlrichs, H. J. Bohm, S. Brode, K. T. Tang, and J. P. Toennies, J. Chem. Phys. **98**, 3579 (1993).

[38] R. Ahlrichs, H. J. Bohm, S. Brode, K. T. Tang, and J. P. Toennies, J. Chem. Phys. **88**, 6290 (1988).

[39] E. F. Archibong, C. Hu, and A. J. Thakkar, J. Chem. Phys. **109**, 3072 (1998).

[40] B. R. Gray, T. G. Wright, E. L. Wood, and L. A. Viehland, Phys. Chem. Chem. Phys. **8**, 4752 (2006).

[41] P. Soldán, E. P. F. Lee, J. Lozeille, J. N. Murrell, and T. G. Wright, Chem. Phys. Lett. **343**, 429 (2001).

[42] P. H. Larsen, H. R. Skullerud, T. H. Lovaas, and Th. Stefansson, J. Phys. B **21**, 2519 (1988).